Electronic structure and defect properties of Tl_6SeI_4: Density functional calculations

Koushik Biswas,[1] Mao-Hua Du,[2] and David J. Singh[2]

[1]*Department of Chemistry and Physics, Arkansas State University, State University, Arkansas 72467, USA*

[2]*Materials Science & Technology Division and Center for Radiation Detection Materials and Systems, Oak Ridge National Laboratory, Oak Ridge, Tennessee 37831, USA*

(Received 15 August 2012; published 8 October 2012)

We report density functional calculations of electronic structure, phase diagram, and dielectric, optical, and defect properties of Tl_6SeI_4. We discuss how electronic structure and defect properties affect resistivity and carrier mobility-lifetime ($\mu\tau$) products in Tl_6SeI_4. We find large Born effective charges due to covalency involving Tl-6p states. High Born charges generally enhance the static dielectric constant. This provides a mechanism for effective screening of charged defects and impurities. We find that high resistivity can be obtained under near-stoichiometric growth conditions via Fermi level pinning near the middle of the band gap by shallow donors and acceptors, as opposed to deep traps that can give high resistivity, but at the expense of short carrier drift lengths. Defect calculations also reveal the presence of deep native donors that may cause electron trapping. The experimentally observed good $\mu\tau$ products may be explained by a combination of small effective masses and effective screening of charged defects. High resistivity and good $\mu\tau$ products make Tl_6SeI_4 a promising room-temperature radiation detector material. We also show the calculated defect diffusion barriers, which affect defect migration under external bias in a detector.

DOI: 10.1103/PhysRevB.86.144108 PACS number(s): 61.72.J−, 71.55.Ht

I. INTRODUCTION

There is a growing need for development of efficient materials for x-ray, γ-ray detection, and isotope identification. This is related to applications in diverse fields including nuclear safeguards, industrial waste characterization, petroleum well logging, and medical diagnostics.[1–3] One of the primary methods of detecting radiation is collection of radiation-generated free carriers in a semiconductor material by applying an external bias. There are several important requirements for room-temperature semiconductor radiation detector materials. These include a large enough band gap (>1.5 eV) to obtain high resistivity at room temperature, but not so large as to lead to poor mobility and reduced numbers of generated electron-hole pairs; good $\mu\tau$ products (μ is the mobility and τ is the lifetime of the charge carriers; this enables charge collection), which are often referred to as the "figure of merit" of the material; high atomic number (Z) of the constituents and large material density for large stopping power of the incident radiation; and high resistivity (>10^9 Ω cm) for minimizing dark current. High resistivity allows the detectors to operate under large bias voltage, which improves charge collection efficiency. One problem with certain otherwise excellent materials is the so-called polarization phenomenon. When this occurs, the external electric field is screened and thus has a short penetration depth in the semiconductor. This is generally due to the accumulation of charged defects and impurities (which diffuse under the external electric field) near electrodes.[4,5] TlBr is an example of a material that exhibits this problem.[6]

Finding good semiconductor radiation detector materials based on all these criteria is a difficult task. Theory suggests that one recipe to obtain high resistivity without significantly compromising carrier transport properties in wide-gap semiconductors is to pin the Fermi level near the middle of the band gap using shallow donors and acceptors and suppress the formation of deep centers.[7–9] Materials that have this type of defect structure are therefore particularly promising. $Cd_xZn_{1-x}Te$ (CZT), which is such a material,[8] is the state-of-the-art room-temperature semiconductor radiation detector material with high resistivity (>10^9 Ω cm) and good electron $\mu\tau$ product (>10^{-3} cm^2/V).[10–14] However, the growth of large-sized high-quality CZT single crystals remains challenging. Many other semiconductor materials have also been studied for their potential applications in radiation detection.[11] In particular, heavy metal halides (e.g., HgI_2, PbI_2, InI, BiI_3, and TlBr) have attracted significant interest because they are high-Z materials and have wide band gaps.[11] Compared to CZT, these heavy metal halides are more ionic and have much softer lattices. This leads to lower melting temperature which can be helpful for single-crystal growth. However, the soft lattice also results in low defect formation energies and high concentrations of native defects.[15,16] Although these halides have high defect concentrations, recent calculations also show that the large Born effective charges and the related large static dielectric constants in Tl, Pb, and Bi halides may reduce the carrier scattering and trapping by charged native defects in these materials.[17,18] This provides a rationale for the observed fact that many heavy metal halides are viable candidates for development as radiation detector materials. Among the binary heavy metal halides, TlBr has emerged as a very promising material with resistivity and electron $\mu\tau$ product both comparable to those of CZT.[19–23] First-principles calculations show that the absence of low-energy deep electron traps may contribute to the good electron $\mu\tau$ product in TlBr,[15] while the presence of such traps may be related to the lagging performance of some other materials, such as InI.[16] Currently, one of the main challenges to the development of the TlBr detectors is the large ionic conductivity,[15,24–28] which results in a severe polarization phenomenon.[29]

More recently, a Tl-based ternary semiconductor material (Tl_6SeI_4) has been proposed as a promising radiation detector material.[30] The Tl_6SeI_4 has a tetragonal structure (space group $P4/mnc$, No. 128, $a = b = 9.178$ Å, and $c = 9.675$ Å),[31] as

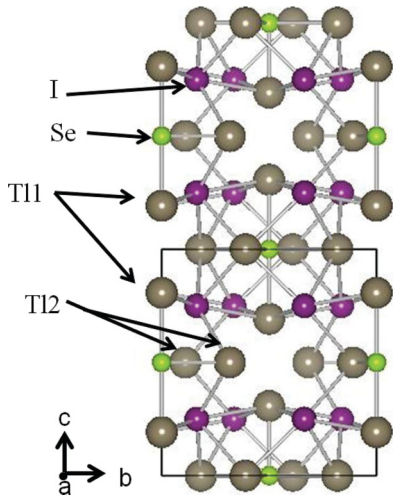

FIG. 1. (Color online) The crystal structure of Tl_6SeI_4. Two distinct sites for Tl ions are shown as Tl1 and Tl2, respectively.

shown in Fig. 1. There are two distinct crystallographic sites for Tl cations. Each Tl^+ ion is coordinated with four I^- ions and one Se^{2-} ion. Tl_6SeI_4 mixes a halide (TlI) with a chalcogenide (Tl_2Se), which in this case results in an intermediate band gap (1.86 eV) between those of Tl_2Se (0.6 eV) and TlI (2.75 eV). Besides having a band gap in the range needed for room-temperature radiation detection, high density, and high average atomic number, Tl_6SeI_4 samples have also exhibited other promising properties, e.g., large $\mu\tau$ products for both electrons (7.1×10^{-3} cm^2 V^{-1}) and holes (5.9×10^{-4} cm^2 V^{-1}), and high resistivity (4×10^{12} Ω cm along the [001] direction).[30]

Actually, ternary chalcohalides may offer several advantages over binary heavy metal halides. Combining chalcogenides and halides enables more flexibility of tuning ionicity/covalency of the material. More covalent bonding character in chalcohalides as compared to halides may reduce the band gap, improve carrier transport, and increase material hardness. A harder lattice may reduce the polarization phenomenon due to higher diffusion barriers for charged defects and impurities. Also, the diffusion of a defect or an impurity usually takes place by hopping of an ion in a specific cation or anion sublattice. In a ternary compound with two types of anions, such as in Tl_6SeI_4, the nearest-neighbor distance for each anion sublattice is usually longer than that in a binary compound. This tends to increase the hopping barrier for defects and impurities on the anion sublattices and consequently reduce the polarization phenomenon. In general, compared to binary compounds, ternary compounds offer wider ranges and flexibility of tuning properties, such as band gap and carrier effective mass. We note that similar considerations apply in other areas, for example, transparent conducting materials, which require both a large band gap and fast carrier transport.[32] However, the flexibility in ternary semiconductors can also come at the expense of more channels for defect formation and more complex defect chemistry, which need to be studied in detail. To better understand the properties of Tl_6SeI_4 in relation to the radiation detection, we performed a first-principles study of electronic structure, phase diagram, and dielectric, optical, and defect properties in Tl_6SeI_4. We will discuss the results in the context of resistivity, carrier transport, and polarization phenomenon in Tl_6SeI_4.

II. METHODS

A. Computational details

We calculated electronic structure, optical absorption, Born effective charges, and defect properties based on density functional calculations. Electronic structure and optical absorption spectra were calculated using hybrid functional calculations (HSE),[33] which produce good band-gap value compared to experimental results. In the HSE calculations, we included 25% nonlocal Hartree-Fock exchange and set the range separation parameter at 0.2. The band gap and the optical absorption spectra were also calculated using Tran-Blaha modified Becke-Johnson potential functional (TB-mBJ) and compared with HSE results. The TB-mBJ is a recently developed functional that has been shown to give good band gaps and optical properties for many semiconductors and insulators but requires much lower computational cost compared to HSE calculations.[34,35] However, it should be noted that TB-mBJ is not a full energy functional and therefore cannot be used for structure relaxation. For the calculations of optical absorption spectra,[36] $4 \times 4 \times 4$ and $8 \times 8 \times 8$ k-point meshes were used for HSE and TB-mBJ calculations, respectively. Convergence tests at Perdew, Burke, and Ernzerhof (PBE) level[37] showed that the $4 \times 4 \times 4$ k-point mesh is converged for the calculations of optical absorption spectra.

Born effective charges and defect properties were calculated using standard PBE generalized gradient approximation (GGA). Density functional calculations based on local density approximation (LDA) and GGA have been extensively used for calculations of defects in semiconductors. The main disadvantage of LDA and GGA is the underestimation of band gaps, which makes it difficult to determine positions of deep defect levels in the band gap. Hybrid functional calculations can correct the band gap and improve the accuracy of the defect calculations[38–43] but also incur high computational cost, especially for calculations of a large number of point defects in large supercells as performed in this work. Interestingly, recent studies show that the deep defect levels calculated using LDA/GGA and hybrid functionals align with each other in the absolute scale.[44–47] This finding justifies the determination of defect level positions relative to band edges by calculating the defect levels using LDA/GGA and then referencing them to band edges corrected by hybrid functional calculations. In this work, the band gaps in the PBE calculations of defects were corrected using the HSE band gap. For this purpose, the HSE band-edge positions relative to those from the PBE calculation were determined by choosing a common reference energy in both calculations, i.e., the average electrostatic potential in the supercell. We used a $2 \times 2 \times 2$ supercell (176 atoms if defect free) and a $2 \times 2 \times 2$ k-point mesh for the defect calculations. Experimental lattice parameters (space group $P4/mnc$, No. 128, $a = b = 9.178$ Å, and $c = 9.675$ Å) were used in all calculations.[31] Using theoretical or experimental lattice parameters should make little difference in defect levels and formation energies,[46] which involve only the calculations of energy differences rather than absolute energies.

TABLE I. Calculated direct band gap in eV at Γ point of Tl_6SeI_4 with PBE, HSE, and TB-mBJ functionals. Values obtained including (SO) and excluding (w/o SO) spin-orbit interactions are given.

Band gap	PBE		HSE		TB-mBJ		
	SO	w/o SO	SO	w/o SO	SO	w/o SO	Experiment[a]
E_g	1.22	1.44	1.74	1.93	1.85	2.02	1.86

[a]Reference 30.

The PBE and HSE calculations were performed using projector augmented wave method (PAW)[48] as implemented in the VASP code.[49] Tl d electrons were included as part of the valence states. The cutoff energy for the plane waves was set at 237 eV and all forces were minimized to below 0.02 eV/Å in structural relaxation calculations. The TB-mBJ calculations were performed using the general linearized augmented plane-wave (LAPW) method as implemented in the WIEN2K code.[50] The WIEN2K calculations were performed using well converged LAPW basis sets plus local orbitals to treat semicore states. The muffin-tin sphere radii employed were $R_{\mathrm{MT}} = 2.7$ bohr for all atoms. The size of the LAPW sector of the basis corresponded to $R_{\mathrm{MT}} K_{\max} = 9.0$.

The PBE, HSE, and TB-mBJ band gaps calculated with and without spin-orbit coupling are given in Table I. The PBE calculations underestimated the band gap as expected while both the HSE and TB-mBJ calculations yielded band gaps in good agreement with the experimental value. The band gaps calculated by VASP and WIEN2K both at PBE level including spin-orbit coupling are in good agreement with each other, i.e., 1.22 eV (VASP) vs 1.27 eV (WIEN2K). This indicates that the two codes are comparable in terms of calculating the band gap with spin-orbit coupling, as also previously found for band-gap calculations for lead chalcogenides.[51]

The defect calculations were performed without the spin-orbit interaction. Spin-orbit coupling gives a somewhat smaller band gap as shown in Table I, but would not in general be expected to significantly change the defect formation energies. We have confirmed this for Tl_6SeI_4 by doing calculations both ways for the case of iodine vacancy where we find that the occupied single-particle level for the negatively charged deep defect and the $(+/-)$ charge transition level inside the band gap have negligible changes upon including spin-orbit coupling. See Sec. II B for details of calculating charge transition levels.

B. Defect calculations

Defect formation energies are given by

$$\Delta H = (\mathrm{E}_D - \mathrm{E}_h) - \sum_i n_i \left(\mu_i + \mu_i^{\mathrm{ref}}\right) + q(\varepsilon_{\mathrm{VBM}} + \varepsilon_f), \tag{1}$$

where E_D and E_h are the total energies of the defect-containing and the host (i.e., defect-free) supercells. Formation of a defect involves exchange of atoms with their respective chemical reservoirs. The second term in Eq. (1) represents the change in energy due to such exchange of atoms, where n_i is the difference in the number of atoms for the ith atomic species between the defect-containing and defect-free supercells. μ_i is the relative chemical potential for the ith atomic species, referenced to its bulk μ_i^{ref}. The third term in Eq. (1) represents the change in energy due to exchange of electrons with its reservoir. $\varepsilon_{\mathrm{VBM}}$ is the energy of the valence-band maximum (VBM) and ε_f is the Fermi energy relative to the VBM. The VBM and the conduction-band minimum (CBM) from the PBE calculation were corrected using the band gap from the HSE calculations as mentioned in Sec. II A. The shallow defect levels, which have mainly the character of bulk electronic states, were shifted with their respective band edges, while the deep levels, which are highly localized, were not corrected since they are not expected to move following the band-gap correction.[44,46,47] Details of these commonly used correction schemes can be found, for example, in Ref. 52. Corrections to the defect formation energy due to potential alignment (between the host and a charged defect supercell) and band filling effects[52,53] were applied wherever appropriate. We did not apply the image charge corrections because there is no experimental result for static dielectric constant. This, however, should not significantly affect our results, given that we used a relatively large 176-atom supercell and that the calculated static dielectric constant of Tl_6SeI_4 is relatively large (see Sec. III A). The transition level of a defect, $\varepsilon(q/q')$, corresponding to a change in its charge state between q and q', is given by the Fermi level, at which the formation energies, $\Delta H(q)$ and $\Delta H(q')$, for charge states q and q' are equal to each other:

$$\varepsilon(q/q') = [\Delta H(q) - \Delta H(q')]/(q' - q). \tag{2}$$

III. RESULTS AND DISCUSSION

A. Electronic structure, Born effective charges, and dielectric and optical properties

The electronic density of states of Tl_6SeI_4 projected onto the two inequivalent Tl sites and the Se and I sites is shown in Fig. 2. The valence-band states of Tl_6SeI_4 are mainly derived from Se-4p, I-5p, and Tl-6s states. The strong hybridization between the Tl-6s and the anion states increases the band dispersion, resulting in a small effective hole mass as was previously reported in Ref. 30. The conduction band is mainly derived from Tl-6p states, which are usually more delocalized

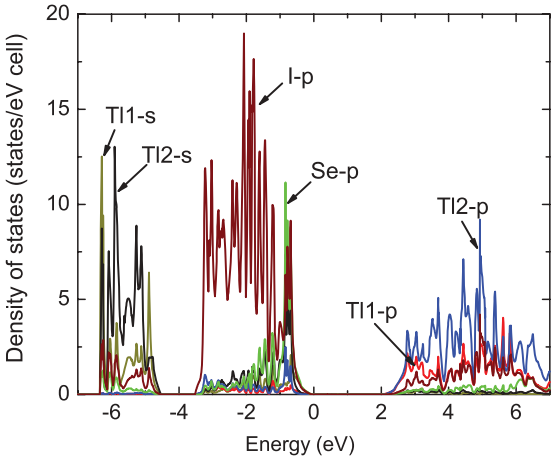

FIG. 2. (Color online) HSE calculated density of states projected on the nonequivalent ions in Tl_6SeI_4.

TABLE II. Born effective charges (Z^*) (calculated using PBE) along a, b, and c directions. Nominal ionic charge on each nonequivalent ion is also shown.

Z^*	Nominal ionic charge	a	b	c
Tl1	1	1.93	1.93	2.05
Tl2	1	1.99	1.99	2.07
Se	−2	−3.22	−3.22	−3.98
I	−1	−2.16	−2.16	−2.06

than the cation-s states commonly found in the conduction bands of compound semiconductors. These characteristics may be related to the good $\mu\tau$ products for both electrons and holes. The cross-band-gap hybridization between the Tl-6p and the anion-p states is also clearly seen in Fig. 2. This results in enhanced large Born effective charges (Z^*) in Tl_6SeI_4 as compared to their respective nominal ionic charges (see Table II). The large Born effective charge as a result of cross-band-gap hybridization has been found in many Tl, Pb, and Bi halides,[17,18] as well as in ferroelectric oxides.[54–57]

Enhanced Born charges indicate strong lattice polarization and are therefore often associated with large static dielectric constant (ε_{st}). The PBE calculated real parts of the anisotropic dielectric function at low frequency are $\varepsilon_{opt}^{XX} = 8.1$ and $\varepsilon_{opt}^{ZZ} = 8.9$, respectively. These values are likely overestimated due to the smaller band gap obtained in PBE. The corresponding values obtained from our HSE calculation are $\varepsilon_{opt}^{XX} = 6.4$ and $\varepsilon_{opt}^{ZZ} = 7.0$, respectively, which are expected to be more accurate than PBE. The ionic contributions to ε_{st}, which depend on phonon frequencies and Born effective charges, were calculated to be $\varepsilon_{ion}^{XX} = 11.7$ and $\varepsilon_{ion}^{ZZ} = 11.2$, respectively, using PBE. We therefore predict a large ε_{st} (∼18) for Tl_6SeI_4. Such a large ε_{st} may provide effective screening of the charged defects and impurities and therefore may reduce the carrier scattering and trapping. This may contribute to large $\mu\tau$ products in Tl_6SeI_4 detectors.

The optical absorption spectra of Tl_6SeI_4 were calculated using both HSE and TB-mBJ functionals. Our calculated band gaps using HSE and TB-mBJ functionals are both in good agreement with experiment (see Table I). Figures 3(a) and 3(b) show a comparison of the anisotropic absorption spectra calculated using HSE and TB-mBJ functionals without spin-orbit coupling. It can seen that HSE and TB-mBJ results are in reasonable agreement with each other. However, the TB-mBJ calculations require much less computational time than the HSE calculations. The optical absorption spectrum taking into account the spin-orbit coupling was then calculated using a TB-mBJ functional [see Fig. 3(c)]. As mentioned, the spin-orbit coupling results in a smaller band gap and thus lower onset of the absorption edge. It can be seen from Fig. 3 that the onset of strong absorption ($>10^4$ cm^{-1}) already occurs at the direct electronic band gap at Γ.

B. Phase diagram of Tl_6SeI_4

We did total energy calculations for Tl_6SeI_4 and competing phases to address the phase diagram, which plays a key role in crystal growth. We find that to obtain stable growth of Tl_6SeI_4 without the formation of other completing phases (e.g., TlI_3, TlSe, Tl_5Se_3, Tl_2Se_3), the relative chemical potentials of Tl, Se, and I in Eq. (1) must be constrained to meet the following conditions:

$$\begin{aligned} 6\mu_{Tl} + \mu_{Se} + 4\mu_I &= \Delta H(Tl_6SeI_4) = -6.764 \text{ eV}, \\ \mu_{Tl} \leqslant 0, \quad \mu_{Se} &\leqslant 0, \quad \mu_I \leqslant 0, \\ \mu_{Tl} + \mu_I &\leqslant \Delta H(TlI) = -1.313 \text{ eV}, \\ \mu_{Tl} + 3\mu_I &\leqslant \Delta H(TlI_3) = -1.472 \text{ eV}, \\ 5\mu_{Tl} + 3\mu_{Se} &\leqslant \Delta H(Tl_5Se_3) = -2.814 \text{ eV}, \\ \mu_{Tl} + \mu_{Se} &\leqslant \Delta H(TlSe) = -0.553 \text{ eV}, \\ 2\mu_{Tl} + 3\mu_{Se} &\leqslant \Delta H(Tl_2Se_3) = -0.799 \text{ eV}. \end{aligned} \tag{3}$$

The calculated heats of formation of the binary compounds shown in Eq. (3) are given per formula unit. The experimental heat of formation of TlI [the only experimental result we found for compounds listed in Eq. (3)] is −1.283 eV/formula unit, in good agreement with the calculated value of −1.313 eV/formula unit.[58] Note that Tl_2Se was said to be used as one of the starting materials for the crystal growth of Tl_6SeI_4.[30] However, Refs. 59 and 60 show that the phase formerly regarded as obeying the formula Tl_2Se actually has a different composition Tl_5Se_3. In the present study we have considered Tl_5Se_3 as a competing phase in the synthesis of Tl_6SeI_4. Figure 4 shows the calculated phase diagram using μ_{Se} and μ_I as two independent variables. μ_{Tl} can be related to μ_{Se} and μ_I using the equation $6\mu_{Tl} + \mu_{Se} + 4\mu_I = \Delta H(Tl_6SeI_4)$ as shown in Eq. (3). The three vertices of the triangle in Fig. 4 denote the limits for Se-rich + I-rich ($\mu_{Se} = \mu_I = 0$, $\mu_{Tl} = -1.127$ eV; vertex A), Se-poor + I-rich ($\mu_{Se} = -6.764$, $\mu_I = \mu_{Tl} = 0$ eV; vertex B), and Se-rich + I-poor ($\mu_I = \mu_{Tl} = 0$, $\mu_I = -1.691$ eV; vertex C) conditions. The shaded region

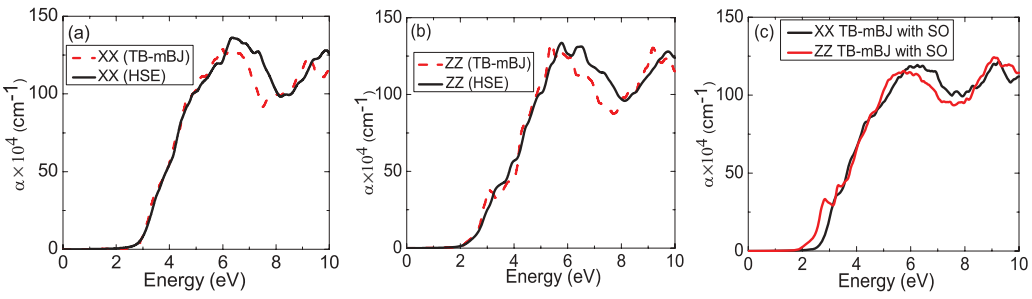

FIG. 3. (Color online) (a) and (b) Comparison of absorption coefficient between HSE and TB-mBJ without spin-orbit interaction. (c) Absorption coefficient calculated using TB-mBJ with spin-orbit interaction.

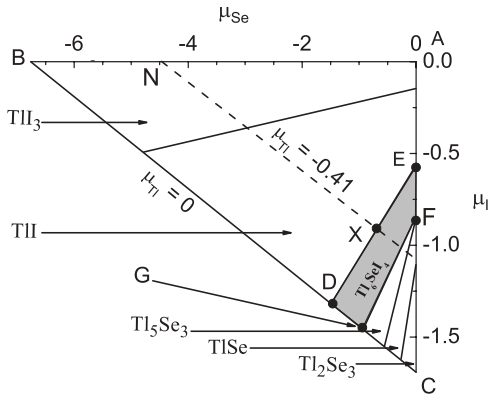

FIG. 4. Calculated ranges of chemical potentials showing the formation of different competing phases under thermodynamic equilibrium. The shaded polygon DEFG is the region where Tl_6SeI_4 is stable without forming other phases.

in the phase diagram (see Fig. 4) corresponds to the ranges of chemical potentials that allow the stable growth of Tl_6SeI_4 without the formation of other competing phases. The regions for other phases are also shown in the phase diagram.

C. Native defects in Tl_6SeI_4

The atomic chemical potential region within the shaded polygon in Fig. 4 is our region of interest where Tl_6SeI_4 is thermodynamically stable. We calculated formation energies of native point defects in Tl_6SeI_4 at the points D, E, F, and G that lie at the boundaries of the phase diagram of Tl_6SeI_4. The line BC in the phase diagram (Fig. 4) corresponds to $\mu_{Tl} = 0$ eV, i.e., the Tl-rich limit. As this line is shifted towards vertex A, the value of μ_{Tl} changes from Tl-rich to Tl-poor regime.

We also calculated formation energies at another point X ($\mu_{Tl} = -0.41$; $\mu_{Se} = -0.69$; $\mu_I = -0.91$ eV. These are roughly the median values of the allowed ranges of chemical potentials of stable Tl_6SeI_4) in the phase diagram of Tl_6SeI_4 shown in Fig. 4. We find that there are five important defects in all cases, i.e., Tl vacancy (V_{Tl}), I vacancy (V_I), Se vacancy (V_{Se}), Se-on-I site (Se_I), and I-on-Se site (I_{Se}). Their formation energies calculated at D, E, F, G, and X points in Fig. 4 are shown in Figs. 5(a)–5(e), respectively. The structure of Tl_6SeI_4 (Ref. 31) has two distinct crystallographic sites for Tl, depicted in Fig. 1 as Tl1 and Tl2. The calculated Se-Tl2 distance is slightly longer (3.08 Å) than the Se-Tl1distance (2.98 Å). The formation energy of neutral V_{Tl} on the Tl2 site is slightly higher than that on the Tl1 site by about 50 meV.

Among the five defects shown in Fig. 5, V_{Tl} and Se_I are shallow acceptors, I_{Se} is a shallow donor, and V_I and V_{Se} are deep donors. Deep donors are deep electron traps and therefore are detrimental to the electron transport. In the Tl_6SeI_4 radiation detector, in which the Fermi level is near

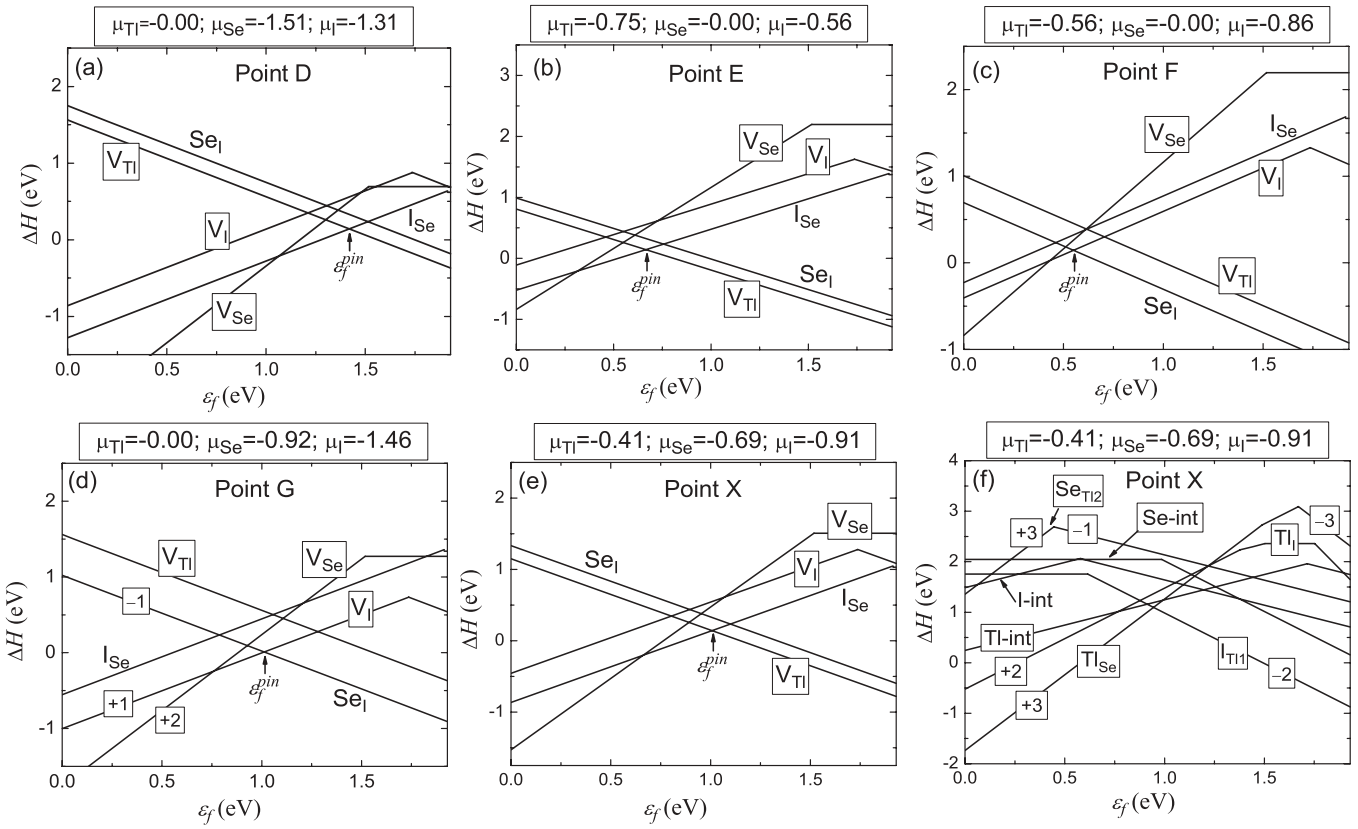

FIG. 5. (a)–(e) Formation energies of important low-energy defects (V_{Tl}, V_I, V_{Se}, Se_I, and I_{Se}) as a function of ε_f at values of chemical potentials that correspond to points D, E, F, G, and X of the stability region of Tl_6SeI_4 shown in Fig. 4. (f) Same for other native defects corresponding to point X of Fig. 4. The slope of the formation energy line indicates the charge state of the defect. The point, where the slope of the formation energy line changes, corresponds to a charge transition level.

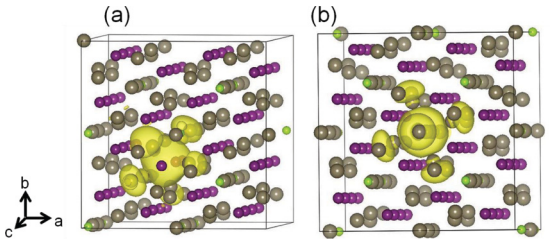

FIG. 6. (Color online) Isosurface plots of the highest occupied localized deep level of (a) V_I^- and (b) V_{Se}^0. The isosurface density is 0.0005 e/bohr^3.

the middle of the band gap, V_I and V_{Se} should be positively charged as V_I^+ and V_{Se}^{2+}, respectively. Our calculations show that both V_I^+ and V_{Se}^{2+} do not induce single-particle levels inside the band gap. However, upon trapping one or two electrons, a defect-induced single-particle level appears inside the band gap. If the level is occupied by two electrons, V_I and V_{Se} become V_I^- and V_{Se}^0, respectively. The deep defect-induced single-particle gap states for V_I^- and V_{Se}^0 are plotted in Fig. 6. In both cases, the defect state is derived from the $6p$ orbitals of the neighboring Tl atoms.

In Fig. 5, the Fermi level is pinned at the point (ε_f^{pin}) where the formation energy lines of the lowest-energy donor and acceptor intersect. Since the points D, E, F, and G in the phase diagram (Fig. 4) are the vertices of the polygon where Tl_6SeI_4 is thermodynamically stable, ε_f^{pin} calculated at these points [see Figs. 5(a)–5(d)] roughly shows the attainable range of ε_f^{pin} in Tl_6SeI_4. It may be seen that ε_f^{pin} is generally in the middle section of the band gap. The point X in Fig. 4 is closer to the stoichiometric condition adopted in material synthesis, and ε_f^{pin} calculated at X point is near the middle of the band gap [see Fig. 5(e)]. These calculations show that high resistivity in Tl_6SeI_4 can be obtained when the starting materials for single-crystal growth correspond to the stoichiometric condition of Tl_6SeI_4.

Besides the native defects shown in Figs. 5(a)–5(e), we have also calculated the formation energies of many other native defects as shown in Fig. 5(f), which correspond to the X point in the phase diagram [Fig. 4]. Although the formation energies of some of these defects are not very high, they are higher than those shown in Fig. 5(e) when the Fermi level is near ε_f^{pin}. Therefore, these defects do not play significant roles in carrier compensation and their impact on carrier trapping is also much less than those shown in Fig. 5(e).

It is desirable to have low concentrations of deep centers in a detector material in order to reduce carrier trapping at defects. One can see from Fig. 5 that the relative stability of the native defects depends sensitively on the chemical potentials. When the chemical potentials correspond to the X point in Fig. 4 (close to the stoichiometric condition), the Fermi level is pinned by a pair of shallow donor and shallow acceptor (I_{Se} and V_{Tl}). This is ideal for the semiconductor radiation detector materials since the shallow donors and acceptors compensate for each other (leading to high resistivity) while not causing significant carrier trapping. However, at ε_f^{pin}, the deep native donors (V_I and V_{Se}) still have relatively low formation energies [see Fig. 5(e)]. Thus these deep donors may exist in appreciable concentration and cause electron trapping. Despite this problem, Tl_6SeI_4 exhibits excellent $\mu\tau$ products.[30] This may be due to a combination of the small effective masses as reported in Ref. 30 and the large static dielectric constant calculated in this work. The electron effective mass along the [001] direction of Tl_6SeI_4 is 0.15 m_o,[30] compared to 0.11 m_o for CdTe (Ref. 10) and 0.51 m_o for TlBr.[27] The calculated static dielectric constant in Tl_6SeI_4 is ∼18, compared to 10.9 in CdTe (Ref. 11) and 30.6 in TlBr.[61,62]

A recent photoluminescence study found a broad emission band at 1.61 eV due to a donor-acceptor pair recombination which was attributed to a shallow donor level at 52 meV below CBM and a deep acceptor level at 290 meV above VBM.[63] Our calculations show that I_{Se} has a donor level at 40 meV below CBM, close to the experimentally observed donor level, but the low-energy native acceptors (V_{Tl} and Se_I) are both shallow and do not show acceptor levels close to 290 meV. However, it is possible that PBE calculations could fail to predict the charge localization associated with the formation of small hole polarons as has been found previously for acceptors in oxides and chalcogenides.[64,65] One possible candidate for the observed donor acceptor pair is the antisite pair (I_{Se}-Se_I), whose formation involves only an interchange of the positions of a Se ion with its nearest-neighbor I ion.

D. Diffusion barrier of low-energy defects

Many of the semiconductor materials that are currently being studied for radiation detection suffer at least to some extent from polarization phenomenon.[4,5,15,29] This may be attributed to ionic conduction which allows the cations, anions, or other defects to migrate to the opposite electrodes creating a field acting against the external bias. Calculation of the barriers of diffusion for charged defects (utilizing a nudged elastic band method with PBE functionals)[66] provides an estimation of how likely the polarization phenomenon will be in a given material.

The crystal structure of Tl_6SeI_4 allows several possible diffusion paths for V_I, V_{Tl}, and Se_I. Figure 7(a) shows the diffusion path of V_I along the c axis and along the ab plane. Se_I has diffusion path similar to V_I. V_{Tl} can migrate via multiple diffusion paths. Along the c axis, it can diffuse along the available Tl2 sites or utilize a combination of Tl1 and Tl2 sites. These two distinct paths are shown in Fig. 7(b) as Tl2→Tl2 and Tl1→Tl2, respectively. The lowest-barrier diffusion path of V_{Tl} on the ab plane is found to be via hopping between adjacent Tl2 sites and is depicted in Fig. 7(c). The calculated diffusion barriers along these different possible paths are shown in Table III. The migration of V_{Se} and I_{Se} is difficult due to the large separation (∼8.1 Å) between adjacent Se sites. We find that there is a metastable state along the diffusion pathway for both defects. This metastable state involves two Se vacancies with one Se interstitial in the case of V_{Se} or with one I interstitial in the case of I_{Se}. The energy differences between the metastable and the ground states for V_{Se} and I_{Se} are shown in Table III. They are 1.65 eV for V_{Se} and 0.94 eV for I_{Se}. The transition states along the diffusion pathway of these two defects (not calculated) should be even higher in energy relative to the ground state. Therefore V_{Se} and

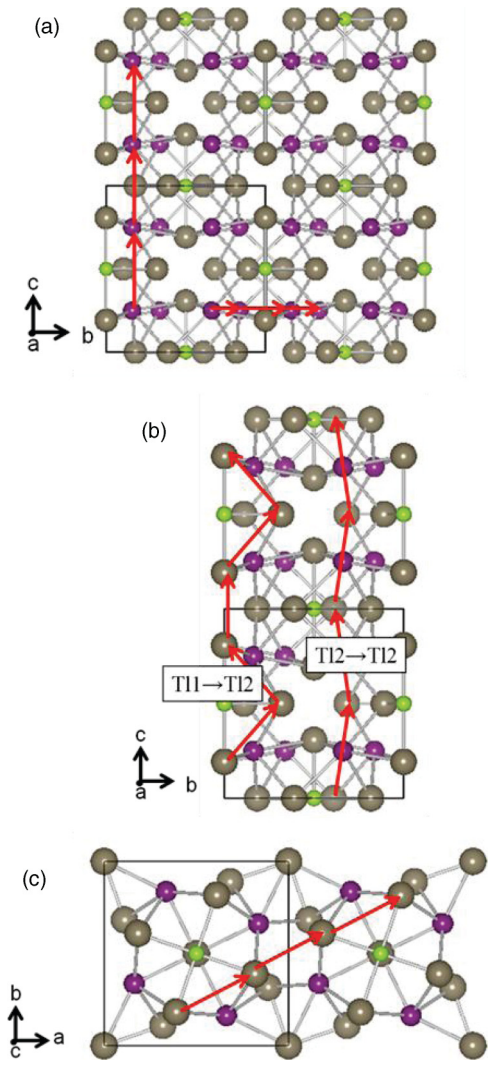

FIG. 7. (Color online) Possible diffusion paths of (a) V_I along the c axis and ab plane, (b) V_{Tl} along the c axis using a combination of Tl1 and Tl2 sites (Tl1→Tl2) or adjacent Tl2 sites (Tl2→Tl2), and (c) V_{Tl} along the ab plane.

I_{Se} should be immobile at room temperature. The calculated diffusion barriers of low-energy charged defects in Tl_6SeI_4 are much higher than those reported for TlBr (0.28 eV for V_{Br} and 0.51 eV for V_{Tl}).[26] Thus, we expect a significantly reduced polarization phenomenon in Tl_6SeI_4 compared to that in TlBr.

TABLE III. Calculated diffusion barrier in eV along the c axis and ab plane of the crystal for different low-energy defects.

	V_I	Se_I	V_{Tl}		V_{Se}	I_{Se}
c axis	0.56	0.68	0.77 (Tl1→Tl2)	1.06 (Tl2→Tl2)	>1.65	>0.94
ab plane	0.89	1.15	0.71 (Tl2→Tl2)		>1.65	>0.94

IV. CONCLUSIONS

We performed first-principles calculations of the electronic structure, phase diagram, and dielectric, optical, and defect properties of Tl_6SeI_4, a promising room-temperature radiation detector material. The calculated large Born effective charges and the resulting large static dielectric constant (∼18) suggest effective screening of charged defects and impurities in Tl_6SeI_4. Defect calculations show that vacancies (V_I, V_{Se}, and V_{Tl}) and antisites (I_{Se} and Se_I) are dominant defects. Among these low-energy defects, I_{Se} is a shallow donor and Se_I and V_{Tl} are shallow acceptors, while V_I and V_{Se} are deep donors. Under near-stoichiometric conditions, the Fermi level can be pinned by the shallow donor I_{Se} and the shallow acceptor V_{Tl} near the middle of the band gap. The compensation between these two defects can lead to high resistivity while not causing deep carrier trapping. However, deep donors (V_{Se} and V_I) may also exist in appreciable concentrations and may cause carrier trapping. The good $\mu\tau$ products reported for Tl_6SeI_4 may be explained by a combination of small effective masses and effective screening of charged defects. The calculated defect diffusion barriers for Tl_6SeI_4 are significantly higher than those for TlBr. This result suggests that the polarization phenomenon in Tl_6SeI_4 should be reduced with respect to TlBr.

ACKNOWLEDGMENT

This work was supported by the US Department of Energy, Office of Nonproliferation Research and Development (NA-22).

[1]B. D. Milbrath, A. J. Peurrung, M. Bliss, and W. J. Weber, J. Mater. Res. **23**, 2561 (2008).
[2]A. Owens, J. Synchrotron Radiat. **13**, 143 (2006).
[3]J. C. McDonald, B. M. Coursey, and M. Carter, Phys. Today **57**, 36 (2004).
[4]D. S. Bale and C. Szeles, Phys. Rev. B **77**, 035205 (2008).
[5]A. Kozorezov, V. Gostilo, A. Owens, F. Quarati, M. Shorohov, M. A. Webb, and J. K. Wigmore, J. Appl. Phys. **108**, 064507 (2010).
[6]K. Hitomi, Y. Kikuchi, T. Shoji, and K. Ishii, IEEE Trans. Nucl. Sci. **56**, 1859 (2009).
[7]M.-H. Du, H. Takenaka, and D. J. Singh, Mater. Res. Soc. Symp. Proc. **1164**, L08-02 (2009).
[8]K. Biswas and M.-H. Du, New J. Phys. **14**, 063020 (2012).
[9]M.-H. Du, H. Takenaka, and D. J. Singh, Phys. Rev. B **77**, 094122 (2008).
[10]T. E. Schlesinger, J. E. Toney, H. Yoon, E. Y. Lee, B. A. Brunett, L. Franks, and R. B. James, Mater. Sci. Eng. **32**, 103 (2001).
[11]A. Owens and A. Peacock, Nucl. Instrum. Methods Phys. Res. A **531**, 18 (2004).
[12]P. J. Sellin, Nucl. Instrum. Methods Phys. Res. A **513**, 332 (2003).
[13]M. Fiederle, V. Babentsov, J. Franc, A. Fauler, and J.-P. Konrath, Cryst. Res. Technol. **38**, 588 (2003).
[14]C. Szeles, IEEE Trans. Nucl. Sci. **51**, 1242 (2004).
[15]M.-H. Du, J. Appl. Phys. **108**, 053506 (2010).
[16]K. Biswas and M.-H. Du, J. Appl. Phys. **109**, 113518 (2011).

[17]M.-H. Du and D. J. Singh, Phys. Rev. B **81**, 144114 (2010).
[18]M.-H. Du and D. J. Singh, Phys. Rev. B **82**, 045203 (2010).
[19]A. V. Churilov, G. Ciampi, H. Kim, L. J. Cirignano, W. M. Higgins, F. Olschner, and K. S. Shah, IEEE Trans. Nucl. Sci. **56**, 1875 (2009).
[20]H. Kim, L. Cirignano, A. Churilov, G. Ciampi, W. Higgins, F. Olschner, and K. Shah, IEEE Trans. Nucl. Sci. **56**, 819 (2009).
[21]M. Shorohov, M. Kouznetsov, I. Lisitskiy, V. Ivanov, V. Gostilo, and A. Owen, IEEE Trans. Nucl. Sci. **56**, 1855 (2009).
[22]T. Onodera, K. Hitomi, T. Shoji, Y. Hiratate, and H. Kitaguchi, IEEE Trans. Nucl. Sci. **52**, 1999 (2005).
[23]K. Hitomi, T. Onodera, and T. Shoji, Nucl. Instrum. Methods Phys. Res. A **579**, 153 (2004).
[24]G. A. Samara, Phys. Rev. B **23**, 575 (1981).
[25]J. Vaitkus, J. Banys, V. Gostilo, S. Zatoloka, A. Mekys, J. Storasta, and A. Žindulis, Nucl. Instrum. Methods Phys. Res. A **546**, 188 (2005).
[26]S. R. Bishop, W. Higgins, G. Ciampi, A. Churilov, K. S. Shah, and H. L. Tuller, J. Electrochem. Chem. **158**, J47 (2011).
[27]S. R. Bishop, H. L. Tuller, G. Ciampi, W. Higgins, J. Engel, A. Churilov, and K. S. Shah, PhysChemChemPhys **14**, 10160 (2012).
[28]C. R. Leao and V. Lordi, Phys. Rev. Lett. **108**, 246604 (2012).
[29]K. Hitomi, Y. Kikuchi, T. Shoji, and K. Ishii, IEEE Trans. Nucl. Sci. **56**, 1859 (2009).
[30]S. Johnsen, Z. Liu, J. A. Peters, J.-H. Song, S. Nguyen, C. D. Malliakas, H. Jin, A. J. Freeman, B. W. Wessels, and M. G. Kanatzidis, J. Am. Chem. Soc. **133**, 10030 (2011).
[31]R. Blachnik, H. A. Dreisbacj, and J. Pelzl, Mater. Res. Bull. **19**, 599 (1984).
[32]G. Trimarchi, H. Peng, J. Im, A. J. Freeman, V. Cloet, A. Raw, K. R. Poeppelmeier, K. Biswas, S. Lany, and A. Zunger, Phys. Rev. B **84**, 165116 (2011).
[33]J. Heyd, G. E. Scuseria, and M. Ernzerhof, J. Chem. Phys. **118**, 8207 (2003).
[34]F. Tran and P. Blaha, Phys. Rev. Lett. **102**, 226401 (2009).
[35]D. J. Singh, Phys. Rev. B **82**, 155145 (2010).
[36]M. Gajdoš, K. Hummer, G. Kresse, J. Furthmüller, and F. Bechstedt, Phys. Rev. B **73**, 045112 (2006).
[37]J. P. Perdew, K. Burke, and M. Ernzerhof, Phys. Rev. Lett. **77**, 3865 (1996).
[38]J. Paier, M. Marsman, K. Hummer, G. Kresse, I. C. Gerber, and J. G. Angyan, J. Chem. Phys. **124**, 154709 (2006).
[39]E. R. Batista, J. Heyd, R. G. Hennig, B. P. Uberuaga, R. L. Martin, G. E. Scuseria, C. J. Umrigar, and J. W. Wilkins, Phys. Rev. B **74**, 121102(R) (2006).
[40]A. Stroppa and G. Kresse, Phys. Rev. B **79**, 201201(R) (2009).
[41]M.-H. Du and S. B. Zhang, Phys. Rev. B **80**, 115217 (2009).
[42]M.-H. Du and K. Biswas, Phys. Rev. Lett. **106**, 115502 (2011).
[43]K. Biswas and M.-H. Du, Appl. Phys. Lett. **98**, 181913 (2011).
[44]A. Alkauskas, P. Broqvist, and A. Pasquarello, Phys. Rev. Lett. **101**, 046405 (2008).
[45]H.-P. Komsa, P. Broqvist, and A. Pasquarello, Phys. Rev. B **81**, 205118 (2010).
[46]H.-P. Komsa and A. Pasquarello, Phys. Rev. B **84**, 075207 (2011).
[47]A. Alkauskas and A. Pasquarello, Phys. Rev. B **84**, 125206 (2011).
[48]P. E. Blöchl, Phys. Rev. B **50**, 17953 (1994).
[49]G. Kresse and J. Furthmuller, Phys. Rev. B **54**, 11169 (1996); G. Kresse and D. Joubert, *ibid*. **59**, 1758 (1999).
[50]P. Blaha, K. Schwarz, G. Madsen, D. Kvasnicka, and J. Luitz, in WIEN2K*: An Augmented Plane Wave + Local Orbitals Program for Calculating Crystal Properties*, edited by K. Schwarz (Technische Universität Wien, Austria, 2001).
[51]K. Hummer, A. Gruneis, and G. Kresse, Phys. Rev. B **75**, 195211 (2007).
[52]S. Lany and A. Zunger, Phys. Rev. B **78**, 235104 (2008).
[53]C. G. Van de Walle and J. Neugebauer, J. Appl. Phys. **95**, 3851 (2004).
[54]R. E. Cohen, Nature (London) **358**, 136 (1992).
[55]W. Zhong, R. D. King-Smith, and D. Vanderbilt, Phys. Rev. Lett. **72**, 3618 (1994).
[56]M. Posternak, R. Resta, and A. Baldereschi, Phys. Rev. B **50**, 8911 (1994).
[57]Ph. Ghosez, J.-P. Michenaud, and X. Gonze, Phys. Rev. B **58**, 6224 (1998).
[58]*CRC Handbook of Chemistry and Physics*, 92nd ed., edited by W. M. Haynes (CRC Press/Taylor and Francis, Boca Raton, FL, 2011).
[59]M. M. Stasova and B. K. Vainshtein, Sov. Phys. Crystallogr. **3**, 140 (1958).
[60]L. I. Man, R. M. Imamov, and S. A. Semiletov, Sov. Phys. Crystallogr. **21**, 355 (1976).
[61]R. P. Lowndes, Phys. Rev. B **6**, 4667 (1972).
[62]R. P. Lowndes and D. H. Martin, Proc. R. Soc. London, Ser. A **308**, 473 (1969).
[63]N. K. Cho, J. A. Peters, Z. Liu, B. W. Wessels, S. Johnsen, M. G. Kanatzidis, J. H. Song, H. Jin, and A. Freeman, Semicond. Sci. Technol. **27**, 015016 (2012).
[64]M.-H. Du and S. B. Zhang, Phys. Rev. B **80**, 115217 (2009).
[65]K. Biswas and M.-H. Du, Appl. Phys. Lett. **98**, 181913 (2011).
[66]H. Jonsson, G. Mills, and K. W. Jacobsen, in *Classical and Quantum Dynamics in Condensed Phase Simulations*, edited by B. J. Berne, G. Ciccotti, and D. F. Coker (World Scientific, Singapore, 1998).